Microscopic Image Analysis for Life Science Applications

Chapter Number	19
Chapter Title	Processing of *In Vivo* Fibered Confocal Microscopy Video Sequences
Author 1	Tom Vercauteren
Author 1 - Address	INRIA Sophia Antipolis, Asclepios Research Group 2004 route des Lucioles, 06902 Sophia Antipolis, France
Author 1 - Email	tom.vercauteren@sophia.inria.fr
Author 1 - Tel	+33 4 92 38 76 60
Author 2	Nicholas Ayache
Author 2 - Address	INRIA Sophia Antipolis, Asclepios Research Group 2004 route des Lucioles, 06902 Sophia Antipolis, France
Author 2 - Email	nicholas.ayache@sophia.inria.fr
Author 2 - Tel	+33 4 92 38 76 61
Author 3	Nicolas Savoire
Author 3 - Address	Mauna Kea Technologies 9 rue d'Enghien, 75010 Paris, France
Author 3 - Email	nicolas.savoire@maunakeatech.com
Author 3 - Tel	+33 1 70 08 09 71
Author 4	Grégoire Malandain
Author 4 - Address	INRIA Sophia Antipolis, Asclepios Research Group 2004 route des Lucioles, 06902 Sophia Antipolis, France
Author 4 - Email	gregoire.malandain@sophia.inria.fr
Author 4 - Tel	+33 4 92 38 79 26
Author 5	Aymeric Perchant
Author 5 - Address	Mauna Kea Technologies 9 rue d'Enghien, 75010 Paris, France
Author 5 - Email	aymeric.perchant@maunakeatech.com
Author 5 - Tel	+33 1 48 24 11 43
Corresponding Author	Tom Vercauteren

Chapter 19

Processing of *In Vivo* Fibered Confocal Microscopy Video Sequences

New imaging technologies allow the acquisition of *in vivo* and *in situ* microscopic images at the cellular resolution in any part of the living body. The automated analysis of these images raises specific issues which require the development of new image processing techniques. In this work, we present some of these issues, and describe some recent advances in the field of microscopic image processing, in particular the automatic construction of very large mosaics from times series of microscopic images to enlarge the field of view. This is also a step to bridge the gap between microscopic and higher resolution images like MRI, PET, SPECT or US. The paper is illustrated with relevant examples for biological or clinical applications.

19.1 Motivations

Cancer is a group of diseases characterized by uncontrolled growth and spread of abnormal cells and is the second leading cause of death worldwide. This simple definition of cancer makes it quite clear that cells play a key role in the different stages of cancer development. Some ninety percent of cancers are preceded by a curable, pre-cancerous and non-invasive stage that progresses without symptoms over a period of years before reaching a cancerous and invasive stage. In the very first step of epithelial cancer, anomalous cells first appear in the deepest layer of the epithelium, directly above the basal membrane. The basal membrane separates the epithelium from the deeper layers of the tissue and provides a very strong and effective protection. It is approximately located at 100 µm deep from the tissue surface for malpighian epithelium, such as cervix epithelium, and 300 µm for glandular epithelium, i.e. tissue that contains secretion glands such as colon, pancreas and thyroid. Because there are no blood vessels in the epithelium, epithelial cells cannot spread to other parts of the body. It is thus important to detect anomalies at a very early stage before the cancer becomes invasive, i.e. before the basal membrane is broken.

Since cancer is a disease that affects cells and starts below the surface of the tissue, its early diagnosis requires a subsurface visualization of the tissue at the cellular level. Current *in vivo* imaging technologies such as MRI, CT, PET, cytometrics, bioluminescence, fluorescence tomography, high-resolution ultrasound or SPECT are only capable of producing images at resolutions between 30 µm and 3 mm. This range of resolution, while largely acceptable for a vast array of applications, is insufficient for cellular level imaging. On the other side of the resolution range, we find several types of microscopy. The vast majority of microscopes, whether conventional or confocal, are limited for use with cell cultures or *ex vivo* tissue samples. The tiny fraction of microscopes that are dedicated to *in vivo* use, and that can function inside the living organism, are called intravital microscopes. These apparatus are cumbersome, difficult to put into use and restricted to research use on small animals. They also require a very delicate and specific preparation of the animal which includes installing a window on the animal body whereby the microscope can look through it into the body.

Since these conventional imaging techniques do not allow for a subsurface cellular visualization of the tissue during a clinical procedure, standard cancer detection protocols are not straightforward. For epithelial cancers, i.e. most cancers affecting solid organs, the current medical diagnosis procedure is to take a tissue sample, or biopsy, and to have it examined under the microscope by a pathologist. Most of these biopsy procedures are performed via endoscopy. An endoscope allows for the visualization of the tissue's surface at the macroscopic level. It can neither see below the surface nor provide a microscopic view of the tissue. Because of this drawback, biopsies have to be performed without a relevant visual guide.

Several systems are today under study to help the endoscopist make an informed decision during the diagnostic endoscopic procedure. Fluorescence spectroscopy can be used to detect dysplasia and early carcinoma based on the analysis of fluorescence spectra [1]. Drawbacks of fluorescence spectroscopy lie in the lack of morphological information, i.e. no cell architecture is available from this modality, and the important rate of false positives due to inflammatory processes. Chromoendoscopy combined with magnification endoscopy has become popular as a diagnostic enhancement tool in endoscopy [2]. In particular, *in vivo* prediction of histological characteristics by crypt or pit pattern analysis can be performed using high magnification chromoendoscopy [3]. One drawback of this technique is that it cannot provide at the same time the macroscopic view for global localization and the zoomed image. Further innovations for better differentiation and characterization of suspicious lesions, such as autofluorescence endoscopy and narrow band imaging are currently under investigation. However for targeting both biopsies and endoscopic resection and improving patient care, the ideal situation is to characterize tissues completely *in vivo*, and thus to visualize cellular architecture. This implies the availability of microscopic imaging during endoscopic examination.

A promising tool to fill this gap is given by fibered confocal microscopy (FCM). The confocal nature of this technology makes it possible to observe subsurface cellular structure which is of particular interest for early detection of cancer. This technology can serve as a guide during the biopsy and can potentially perform optical biopsies, that is, a high resolution non invasive optical sectioning within a thick transparent or translucent tissue [4].

19.2 Principles of Fibered Confocal Microscopy

The ideal characteristics or specifications of a system dedicated to optical biopsies are numerous. The resolution should not exceed a few microns to make it possible to distinguish individual cells and possibly sub-cellular structures. Above all, the system should be easy to operate, in complete adequateness with the current clinical practice. It should not modify the clinician's procedure and practice. Following a short learning curve due to the manipulation of a new instrument and to the interpretation of images never obtained before in such conditions, no more adaptation should be needed in the clinical setting. In particular, the parts of the system meant to be in contact with the patient should be easily disinfected, using standard existing procedures. Such characteristics are crucial for the development of a system designed to be used in routine practice and not only for clinical research purposes.

19.2.1 Confocal microscopy

Confocal microscopy enables microscopic imaging of untreated tissue without previous fixation and preparation of slices and thus meets some of the operational ease requirements as well as the resolution requirement. The technical principle is based on point-by-point imaging. In a laser scanning confocal microscope a laser beam is focused by the objective lens into a small focal volume within the imaged sample. A mixture of emitted fluorescence light as well as reflected laser light from the illuminated spot is then recollected by the objective lens. The detector aperture obstructs the light that is not coming from the focal point. This suppresses the effect of out-of-focus points. Depending on the imaging mode, the detector either measures the fluorescence light or the reflected light. The measured signal represents only one pixel in the resulting image. In order to get a complete image and perform dynamic imaging, the imaged sample has to be scanned in the horizontal plane for 2D imaging as well as the vertical plane for 3D imaging.

Confocal microscopy can be adapted for *in vivo* and *in situ* imaging by, schematically, inserting a fiber optics link between the laser source and the objective lens.

19.2.2 Distal scanning fibered confocal microscopy

First attempts for developing fibered confocal microscopes (FCM) have historically been made by teams coming from the world of microscopy. The well known constraints of confocal microscopy were directly transposed to specific architectures for new *endomicroscopes*. With a similar technological core, these designs were in majority based on distal scanning schemes where one fiber serves at the same time as a point source and a point detector. Different architectures have been investigated by several academic groups and commercial companies: distal fiber scanning, distal optical scanning and MEMs distal scanning. The great advantage of this technology is illustrated by its very good lateral resolution: almost that of non-fibered systems. The systems developed by Optiscan [5], Olympus [6], Stanford University [7] and others produce very crisp images through only one optical fiber. These systems have first been driven by technological solutions already existing in the microscopy field. Their ability to obtain high resolution images is one of their strengths. However, image quality is just one clinical requirement among many different needs absolutely necessary for performing *in vivo* microscopic imaging. Other needs include miniaturization, ease of use and real time imaging. One can point out that distal scanning solutions are not able to meet all the demands of a clinical routine examination. Even if they are considered as very good imaging solutions, they are often relatively invasive, do not allow for real-time imaging and are not fully integrated within the current medical routine.

19.2.3 Proximal scanning fibered confocal microscopy

To circumvent the problems of distal scanning FCM, a number of teams have tried to use a proximal scanning architecture [8, 9]. In this work, we use a second generation confocal endoscopy system called Cellvizio® developed by Mauna Kea Technologies (MKT), Paris, France. MKT's adaptation of a confocal microscope for *in situ* and *in vivo* imaging in the context of endoscopy can be viewed as replacing the microscope's objective by a flexible optical microprobe of length and diameter compatible with the working channel of any flexible endoscope. For such purpose, a fiber bundle made of tens of thousands of fiber optics is used as the link between the proximal scanning unit and the microscope objective, remotely placed at the tip of the flexible optical microprobe. The schematic principle of fibered confocal microscopy is shown in Fig. 19.1 and typical images are shown in Fig. 19.2.

Such a choice has many advantages on the applicative side [10, 11]. Decoupling the scanning function from the imaging one allows the optimization of both functions independently. The distal optics can thus be miniaturized down to a volume much smaller than what distal scanners can reach now, with very little compromise between optical quality and size. Since the scanner can be allocated an arbitrary volume, well known and reliable rapid scanning solutions such as resonant or galvanometric mirrors can be used. A purely passive optical microprobe is also more compatible with any cleaning or decontamination procedure that regular clinical use requires. Last but not least, fiber bundles are already existing products, available on the market under different designs and specifications, with no need of specific developments for their use in medical devices. Their association with simplified distal ends enable their manufacturing at a relatively low cost, opening the way to the production of disposable items.

Cellvizio® makes it possible to observe subsurface cellular structures with an optical section parallel to the tissue surface at a depth between 0 and 100 µm. The imaging depth cannot be controlled on a single optical microprobe but depends on the specific optical microprobe used. Therefore, the physician will be using different optical microprobes, with different technical specifications, for different applications. Confocal image data is collected at a frame rate of 12 frames per second. Smallest lateral and axial resolutions are 1 µm and 3 µm respectively. Fields of view ranging from 130×130 µm to 600×600 µm can be obtained thanks to a set of flexible optical microprobes with diameters varying from 0.16 to 1.5 mm. These microprobes can be inserted through the working channel of any endoscope. Note that since the FCM is typically used in conjunction with an endoscope, both macroscopic (endoscope image) and microscopic view (FCM image) can be obtained at the same time. This is illustrated in Fig. 19.3. This dual-view facilitates the selection of the area to be biopsied.

Of course, this approach has well known drawbacks. Proper light focusing and collection at the distal end of the probe is simplified by the absence of distal scanning means but remains a critical issue. This is particularly true when reaching very small optics dimensions. Because of the passivity of the fiber optics bundle, the system also suffers from some loss of resolution and is limited to 2D imaging. However, the most widely reported problem of this approach is certainly related to the image itself. It often suffers from artifacts, aliasing effects and, most importantly, always shows a strongly visible honeycomb pattern.

In the sequel, we show that specific image processing schemes can be designed to cope with these artifacts in real-time. The control and acquisition software that comes with the Cellvizio® is thus an inherent part of the imaging device and helps it move towards a true optical biopsy system. Such a real-time reconstruction algorithm provides smooth-motion video sequences that can be used for more advanced image processing tasks. Figure 19.4 illustrates some of the image processing challenges we address in this chapter. After the presentation of our real-time fiber pattern rejection scheme in Section 19.3, we will focus on three advanced image processing tasks. Namely, the measurement of blood flow from single images, the stabilization of a specific region of interest and the construction of wide field of view image mosaics.

19.3 Real-time Fiber Pattern Rejection

The specific imaging modality we focus on raises specific image processing problems. The non-uniform honeycomb pattern and the geometric distortions that appear on the raw data, makes it impracticable for user interpretation or for automated analysis if left untreated. Algorithms that take on the image reconstruction task in real-time have thus been developed. They provide users with high-quality, smooth-motion video sequences. These are effortlessly interpretable by the professionals who rely on them for diagnosis and readily usable for further automated image processing and analysis. Most of the available methods are only focused on the removal of the honeycomb pattern [12, 13] and often only imply performing a simple low-pass filtering. Our approach in [14] not only removes the honeycomb pattern but also recovers the true signal that comes back from the tissue and removes the geometric distortions.

19.3.1 Calibrated raw data acquisition

Proximal implementation of the scanning function enables the use of very robust and reliable solutions for a fast and accurate scanning. The laser scanning unit performs a scanning of the proximal surface of the flexible optical microprobe with the laser source by using two mirrors. Horizontal line scanning is done using a 4 kHz oscillating mirror while a galvanometric mirror handles frame scanning at 12 Hz. A custom synchronization hardware controls the mirrors and digitizes, synchronously with the scanning, the signal coming back from the tissue using a mono-pixel photodetector. Cellvizio® scanning reproducibility is better than one half of a fiber diameter. This performance first enables the calibration of the continuous motion of the illuminating spot. It allows to compensate for the sine-wave shape of the field distortion due to the resonant mirror (fisheye-like effect), and permits a comprehensive rectangular mapping of the field of view. This is mandatory for any further interpretation of the metrics of the images, or any complex combination of individual frames. Second, the proximal scanning is associated with optimized optics that guarantees a very good injection of the laser within the fibers.

When organized according to the scanning, the output of the FCM can be viewed as a raw image of the surface of the flexible optical microprobe. Scanning amplitude and signal sampling frequency have been adjusted to perform a spatial over-sampling of the fiber bundle. This is clearly visible on the raw image in Fig. 19.5 where one can see the individual fibers composing the bundle. Such an oversampling is needed to distinguish the signal coming from each individual fiber. A typical fiber bundle is composed of $30,000$ fiber optics, with a fiber inter-core distance d_{ic} of 3.3 µm, and a fiber core diameter of 1.9 µm. Fiber arrangement is locally quasi hexagonal, but does not show any particular order at larger scales.

Critical elements in the raw image formation process lie in a correct spatial sampling of the flexible optical microprobe but also in the adjustment of the point spread function (PSF) of the system with this spatial sampling. We indeed want to avoid aliasing on the tissue side. When analyzing the system from the point of view of the sampling theory, the PSF corresponds to the low pass filter and the fiber optics bundle to the sampling grid. The Nyquist frequency is then given by $(M/d_{ic})/2$ where M is the magnification of the optical head and typically ranges from 1.0 to 2.5. The PSF of the system must therefore satisfy this frequency. As a rule of thumb the PSF width should approximately be the Nyquist period. The resulting lateral resolution of such a system is then given by $2 * d_{ic}/M$. For a user to benefit from the full spatial resolution allowed by the sampling theorem, an optimal fiber pattern rejection and geometric distortion compensation scheme is needed.

19.3.2 Real time processing

The task of the on-the-fly image reconstruction module is to restore, at a rate of 12 frames per second, the true physical signal from the raw data by removing the fiber bundle honeycomb modulation and the scanning distortion. Each fiber of the bundle provides one and only one sampling point on the tissue. Associated with these sampling points comes a signal that depends on the imaged tissue and on the single fiber characteristics. The role of the image processing is first to build a mapping between the FCM raw image and the fibers composing the flexible optical microprobe. Once this mapping is obtained, characteristics of each fiber are measured and the effective signal coming back from the tissue is estimated. We then have non-uniformly sampled frames where each sampling point corresponds to a center of a fiber in the flexible optical microprobe. An interpolation algorithm is then used to provide the user with smooth images. Let us now provide some details for each of these steps.

Calibration – As a preliminary step, we build a mapping between the FCM raw image and the fibers composing the flexible optical microprobe. This is achieved by using a segmentation algorithm specifically designed for our fiber optics bundle. Since we now have access to the position of the fibers within the raw image and to the scanning distortion, it becomes possible to get a point set with the exact, distortion-free, positions of the fibers in the bundle.

This mapping allow us to compute the signal measured by a single fiber. When combined and averaged together, the almost 15 to 50 pixels corresponding to one single fiber lead to a signal I with a much better SNR.

Since the signal that is measured by a single fiber depends on the imaged biological sample fluorescence α_{fluo} and on the fiber itself, we need to estimate some characteristics of each single fiber such as its gain and autofluorescence. For this purpose, we acquire an image of a non-fluorescent sample, $\alpha_{fluo} = 0$, and compute the background signal I_b measured by each fiber. We also acquire an image of a sample of constant fluorescence, $\alpha_{fluo} =$ cst, and compute the signal I_s associated to each fiber.

Imaging Model – To represent the relationship between the actual biological sample fluorescence of interest α_{fluo} and the raw signal I measured by each fiber of the flexible optical microprobe, we use the following model from [14]:

$$I = I_0 \cdot \big(a \cdot \tau_{inj} \cdot \tau_{col} \cdot \alpha_{fluo} + b \cdot \tau_{inj} \cdot \alpha_{autofluo}\big) \tag{19.1}$$

where a and b are constants, τ_{inj} and τ_{col} are the injection rate and collection rate of the fiber, $\alpha_{autofluo}$ is the intrinsic auto-fluorescence of the fiber, and I_0 is the intensity of the laser source.

Given the raw signal and the calibration data, the true physical measure α_{fluo} we would like to have cannot be directly estimated. It is however possible to recover it up to a scaling factor with the following equation:

$$I_{restored} = \frac{I - I_b}{I_s - I_b} = K \cdot \alpha_{fluo}, \tag{19.2}$$

where K is a constant independent of the considered fiber.

Reconstruction – At this step, we have a restored intensity $I_{restored}$ for each fiber composing the image bundle. The final process is the interpolation or approximation of this point set into an image on a square grid. The simplest method uses a nearest-neighbor scheme where all pixels within the area of one fiber are assigned a common value. Other usual algorithms for scattered data interpolation or approximation, such as triangulation based methods, kriging methods, radial basis functions interpolations, B-Spline approximations, natural neighbors or moving least squares methods (see e.g. [15–17] and references therein) can also be used depending on the required smoothness, approximation order, efficiency and other numerical issues. We found that for real time applications, a linear interpolation on triangles provided a good compromise between visual appearance and computational requirements.

19.4 Blood Flow Velocimetry using Motion Artifacts

The analysis of the behavior of blood cells and vessels is a very important topic of physiology research. As such, *in vivo* measurements made for example by intravital fluorescence microscopy have proved since the early seventies to be crucial to the understanding of the physiology and pathophysiology of microcirculation. More recently, fibered confocal microscopy has been shown to allow for the observation and measurement of several characteristics of microcirculation with the clear benefit of reducing the invasiveness to its bare minimum [18].

However, as for any quantitative measurement from images, the automated analysis of the data poses a number of new challenges that need to be addressed with specific solutions. In this section we show an image processing algorithm proposed in [19] dedicated to the velocimetry of blood flow imaged with FCM.

19.4.1 Imaging of moving objects

An interesting point of scanning imaging devices is that the output image is not a representation of a given instant, but a juxtaposition of points acquired at different times [19]. Consequently, if there are objects in the field of view that are moving with respect to the flexible optical microprobe, what we observe is not a frozen picture of these objects, but a skewed image of them. Each scan line indeed relates to a different instant, and the objects move between each scan line.

From the analysis of the laser scanning in Section 19.3.1, it is seen that the scanning movement can be decomposed into a fast horizontal sinusoidal component and a slow linear uniform vertical component. Horizontally, the imaging is done only on the central part of the trajectory, where the spot velocity is maximal and nearly constant. Since in this part, the spot horizontal velocity V_x (> 5 m/s) is several orders of magnitude higher than both the spot vertical velocity V_y (~ 2 mm/s) and the velocity V_c of observed red blood cells (RBC) (< 50 mm/s), two approximations can be made: the scan lines are horizontal and the time needed by the spot to cross the imaged part is negligible, meaning that the objects are considered motionless during a scan line. This amounts to assuming that the horizontal spot velocity is infinite.

Let us consider a standard 2D+t volume $V(x, y, t)$. Without scanning, this volume will be imaged by 2D slices $V(x, y, t_0)$ at different instants t_0. With scanning, the process of image formation comes down to imaging the plane $V(x, y, t_0 + y/V_y)$. Figure 19.6a presents what will be observed when imaging a vertical segment moving horizontally with respect to the flexible optical microprobe.

19.4.2 Velocimetry algorithm

Classical methods for velocity measurements of blood cells in microvessels are often based on the processing of 2D temporal image sequences obtained in the field of intravital microscopy. Line shift diagram, spatio-temporal analysis or blood cell tracking are used in such setting to process the sequences generated by CCD-based video microscopes [20].

In contrast, the method presented in [19] uses very specific information about the imaging device. By the combination of its own movement and the laser scanning, a red blood cell should appear almost as a slanting segment, whose length and orientation with respect to the scanning and the microvessel are dictated by its velocity. This specificity can be used to measure the velocity of blood cells in microvessels from single images. The method exploits the motion artifacts produced by the laser scanning. Although velocity can be estimated from a single image, temporal sequences can then be exploited to increase the robustness and accuracy of the estimation.

To get an idea of how the algorithm works, we model a imaged red blood cell as a disk of radius R. This assumption is rather realistic since the diameter of a typical mammal RBC is 5–9 μm and can thus only be seen by a few fibers in the flexible optical microprobe. Let us assume that the RBC has a linear uniform movement described by a velocity V_c and a trajectory angle θ. Let us also assume that the RBC is imaged by a scanning laser whose horizontal velocity is infinite and vertical velocity is V_y so that the disk will be distorted by the scanning imaging.

Let us look at the equation of the distorted envelope, i.e. the intersection between the disk envelope and the scanning spot. The points (x_c, y_c) of the envelope of the disk at the instant t verify the equation:

$$\frac{(x_c - V_c \cdot t \cdot \cos\theta)^2}{R^2} + \frac{(y_c - V_c \cdot t \cdot \sin\theta)^2}{R^2} = 1 \tag{19.3}$$

The vertical position y_s of the spot is given by $y_s = V_y t$. The horizontal spot velocity is supposed infinite, which is why the intersections of the spot trajectory and the envelope are the intersections of the envelope with the line of ordinate y_s. Using $t = y_s/V_y$ in (19.3), we see that the distorted envelope is in fact an ellipse. The moving disk will thus appear as an ellipse in the output image. The angle α (modulo $\pi/2$) and length L of the major ellipse axis are given by:

$$\tan 2\alpha = \frac{2\cos\theta}{V_r - 2\sin\theta}, \tag{19.4}$$

$$L = \frac{2R\sqrt{2}}{\sqrt{V_r^2 - 2V_r \cdot \sin\theta + 2 - V_r\sqrt{V_r^2 - 4V_r \cdot \sin\theta + 4}}}, \tag{19.5}$$

with $V_r = V_c/V_y$.

Equations (19.4) and (19.5) link the velocity and angle θ of the moving disk to the observed values L and α. Given L and α, the inversion of the relations gives two possible solutions for V_c and θ. This implies that a single output image only allows to retrieve the velocity and trajectory angle of the disk with an ambiguity between two possibilities. The ambiguity could be removed by considering two scans, one top-down and another bottom-up for example.

One difficulty lies in using L because extracting individual shapes in images like the ones of figure 19.6b seems unlikely. Only the orientation α can be retrieved, which forbids the use of (19.5). The solution is to suppose that the angle of trajectory θ is known (for example in image 19.6b, the trajectory of the RBCs is supposed colinear to the edges of the vessel). With this hypothesis, (19.4) allows for the determination of the disk velocity.

From the images, it is clear that the segmentation of individual traces is not possible. In fact, in Fig. 19.6b as the plasma is marked by a fluorescent dye, distorted RBC shapes are expected to appear as dark trails. But what we observe seem to be bright trails. Our explanation is that there are so many dark trails that it induces a contrast inversion. Given the RBC blood concentration, i.e. 4–5 million per microliter of blood, about 1000 RBCs should be in this image. What we see are thus the bright interstices between the dark trails. It is the slope of these white ridges that we extract from the images in order to estimate the velocity through the orientation of the ridges. The extraction algorithm itself is based on a combination of ridge detection and robust estimators.

Our algorithm assumes that the ridges are tubular-like structures with a Gaussian profile of standard deviation σ_0. It proceeds in four steps. First, we enhance the horizontal edges by computing the vertical gradient component $I_y(x, y)$ of the image I. Since ridges are composed of points that are at equal distance of a positive gradient response and a negative gradient response, the medialness response $R(x, y) = I_y(x, y + \sqrt{\sigma_0^2}) - I_y(x, y - \sqrt{\sigma_0^2})$ of [21] should be maximal on the ridges. Our second step uses a high threshold on $R(x, y)$ to compute regional maxima on each connected component of the thresholded image. In the third step, regional maxima are used as seeds to extend the ridges. This extension is done by following the local maxima of $R(x, y)$ until a low threshold is reached. This approach is similar to doing a hysteresis thresholding in a privileged direction. Finally, a line is robustly fitted on each extracted ridge to measure the slope.

19.4.3 Results and evaluation

In the field of biomedical imaging, the issue of validation for image processing tasks is essential but is often a difficult problem that needs very specific approaches in order to be addressed. In this work several experiments have been conducted to estimate the correctness of the method. First a numerical simulator was developed. It models the acquisition of the Cellvizio® and simulates a simple laminar flow of RBC where RBC are represented by a realistic 3D model that departs from the disk model we used for the theoretical part. RBC velocities are randomly set according to a normal distribution. Applying the proposed method and taking the median of the estimated velocities leads to a velocity estimation within a 6% margin error. Secondly, we applied our method to a sequence of 40 images obtained on real acquisitions of mouse cremaster microvessel. For each image, we computed the median of estimated velocities. Since the actual velocity of RBC in the vessel is unknown, we cannot estimate the correctness of the estimation, nevertheless this allows us to test the stability and robustness of the method. For the whole sequence, the mean of the median velocity of each image is 7.18 mm/s and the standard deviation is 0.7 mm/s. This result tends to prove that our velocity estimation is robust and stable along the sequence. Our most advanced validation experiment uses an in-house built hydraulic circuit. Water with fluorescent balls, whose size is comparable to a RBC, flows in this circuit and the flow velocity is adjustable. This system lets us compare our velocity estimations with the velocity computed from the rate of flow of the circuit. This serves as a validation of our method. We do not have access to the precision of the velocity computed from the rate of flow but both methods agree with a mean relative error of 16%.

Our velocimetry method has been applied, in Fig. 19.6b, to a real acquisition of mouse cremaster microvessel. The image is divided into a set of blocks. For each block, a robust estimation of the velocity is computed. We can see that our method is able to recover the red blood cell velocity profile within the microvessel. As expected, the velocity does not change along the direction of the microvessel and is maximal at the center.

As this approach is based on a line scan interaction between the laser scanning and the moving cells, higher velocity can be measured than with methods based on analysis of successive temporal frames. When most systems are limited to the measurement of red blood cell velocity inferior to 2 or 5 mm/s, the presented method allows the measurement of velocities up to 30 mm/s.

19.5 Region Tracking for Kinetic Analysis

The high resolution images provided by Cellvizio® are mostly acquired on living organs, therefore specific image processing tools are required to cope with the natural movements of the tissues being imaged. Moreover, if the images of a sequence were stabilized, measurements of various image parameters would become possible or easier and could be carried out for many applications such as gene expression monitoring, drug biodistribution or pharmacokinetics.

Due to the very specific type of images generated by Cellvizio®, classical image stabilization and registration techniques could not be applied here. As a result, we have developed a dedicated region of interest (ROI) tracking tool that takes into account the characteristics of Cellvizio®, and enables an automatic registration, analysis and quantification on sequences of images [22].

In Section 19.4, we have shown that the motion of the imaged objects with respect to the optical microprobe led to some motion artifacts. The velocimetry took advantage of these artifacts to enable blood flow measurement. However in most cases motion artifacts would simply induce possible misquantifications. A high frame rate can sometimes compensate for the resulting distortions but when the frame rate cannot be increased, motion artifacts can in general not be avoided. We show here that the knowledge we have about the motion distortion can also be used to get an efficient motion compensation algorithm. We address the case where a user wants to focus on a small region of the living tissue that is difficult to stabilize mechanically. For instance, *in vivo* and *in situ* acquisition on the liver, the bladder or even the heart can be unstable. Such organs receive a growing interest among biologists to assess pharmaco-kinetics parameters of molecules, to screen the changing morphology of the anatomy, or to measure bio-distribution parameters.

19.5.1 Motion compensation algorithm

Let us suppose that the motion of the imaged object with respect to the optical microprobe between two contiguous frames is a simple translation at speed $\tilde{\eta} = [\tilde{\eta}^x, \tilde{\eta}^y]$. A scanned line with vertical position y, will be sampled at the time $t(y) = t(0) + \frac{y}{V_y}$. During the scanning, a point $p = [x, y] \in I$ in the image coordinate system will be sampled at position $p_d = [x_d, y_d]$ in the object coordinate system. We note $\eta = \frac{\tilde{\eta}}{V_y}$ the normalized speed for the frame scanning. The position p_d of the imaged object point is given by:

$$x_d = x + (t(x) - t(0))\tilde{\eta}^x = x + \frac{y}{V_y}\tilde{\eta}^x = x + \eta^x y,$$
$$y_d = y + (t(y) - t(0))\tilde{\eta}^y = y + \frac{y}{V_y}\tilde{\eta}^y = (1 + \eta^y)y.$$

For the k^{th} frame, this linear transformation between the image coordinate system and the object coordinate system is noted v_k. Each point p of a frame I_k is mapped to a reference space coordinate system by the transformation $f_k : p \rightarrow p_{ref}$ such that

$$f_k(p) = r_k \circ v_k(p),$$

where r_k is a rigid body transformation and $\circ$ denotes the composition of spatial transformations. Between two frames j and k, the spatial transformation is thus given by:

$$f_{j,k}(p) = v_j^{-1} \circ r_j^{-1} \circ r_k \circ v_k = v_j^{-1} \circ r_{j,k} \circ v_k. \qquad (19.6)$$

In order to recover the alignment between the images and the motion distortions, one could try to register the frames using the complete transformation model above. However, this would imply to ignore the relationship between positions and velocities and would thus not really be robust. We therefore choose to compute the velocities using the displacements information only. Using finite difference equations, we can relate the global positioning and the velocity η. The estimation of the velocities is done using only the translation part of $r_{j,k}$. This velocity is used in the following algorithm to compensate for the scanning distortions. For each contiguous frames the following steps are performed:

1. Estimate the translation using a 2D normalized cross correlation,
2. Estimate the velocity from the translation,
3. Compute the distortion transformation,
4. Optimize the rigid transformation.

19.5.2 Affine registration algorithm

Using Cellvizio®, the handheld optical microprobe can freely glide along the soft tissue while keeping contact with it. The spatial transformation between two frames will thus be composed of a translation, a possible rotation, and even a little scaling if the tissues are compressed. Another representation of the frame to frame spatial transformation is thus given by an affine transformation model which is a generalization of the model in (19.6).

The image registration scheme we use is based on a minimization of the sum of squared differences between the intensities of the current image I_k and a reference image I: $\sum_p |I(p) - I_k(f_k(p))|^2$, with f_k being an affine transformation. To ensure a fast convergence in the optimization procedure, we initialized each transformation by the best translation found by a normalized cross correlation and use a fast and efficient optimizer. The efficient second order minimization (ESM) scheme of [23] provides excellent results for real time robotic applications. We have adapted it to use an affine transformation instead of a projective one [24]. The main advantage of this algorithm is to provide a true second order optimization scheme with the complexity of a first order optimization scheme such as Gauss-Newton. Of course, other optimizers could be used.

19.5.3 Application to cell trafficking

In [22], this ROI tracking was used to assess cell trafficking in a capillary. The aim is to measure a slow blood velocity in a capillary. For this range of blood velocity and this size of capillary (as small as a single RBC), the previous velocimetry algorithm could not be used since single RBC can be seen on the images. On the other hand, more conventional methods using temporal image sequences could not directly be used because of the unstable nature of many imaged tissue such as tumoral grafts. This is why we choose to first track a given region of interest and then use a cross-correlation scheme on the stabilized sequence. The user can select manually a rectangular ROI on the image. Fig. 19.7a shows the tracking of this region on a sequence acquired with a hand-held probe on a tumoral skin xenograft. Vessels were stained using dextran fluorescein from Invitrogen.

On the temporal mean frame of the stabilized sequence, we have segmented the vessels using a 2D adaptation of the multi-scale tubular vessel detection algorithm of [21]. We used this same adaptation on the same type of images in [25] to perform morphometric analysis of the vascular network. The upper left image of Fig. 19.7b shows the result of the detection: the medial axis and the vessel borders. The medial axis of the vessel in the ROI was used to extract the vessel intensity in the center line. The normalized cross correlation of these two lines allows for the estimation of the velocity of the blood in the capillary.

The range of velocities that can be addressed depends on the scanning period, and amplitude. We here give some typical values for Cellvizio®. The velocity precision is given by the minimum translation observable between two frames: $\delta v = 0.02$ mm/s. The velocity interval computed using a maximum detectable translation of half the horizontal field of view is $[0, 7.2]$ mm/s.

An additional interesting feature of this tracker is that it also enables the reconstruction of images on the region of interest with an enhanced resolution. This is made possible, when the kinetic of the signal is slow enough, thanks to the noise reduction provided by the processing of several registered noisy images of the same region and to a small remaining aliasing of the input images.

19.6 Mosaicing: Bridging the Gap between Micro and Macroscopic Scales

We showed that fibered confocal microscopy can unveil in real-time the cellular structure of the observed tissue. However, as interesting as dynamic sequences may be during the time of the medical procedure or biological experiment, there is a need for the expert to get an efficient and complete representation of the entire imaged region. A physician needs, for example, to actually add still images in the patient's medical record.

Image sequence mosaicing techniques are used to provide this efficient and complete representation and widen the field of view (FOV). Several possible applications are targeted. First of all, the rendering of wide-field micro-architectural information on a single image will help experts to interpret the acquired data. This representation will also make quantitative and statistical analysis possible on a wide field of view. Moreover, mosaicing for microscopic images is a mean of filling the gap between microscopic and macroscopic scales. It allows multi-modality and multi-scale information fusion for the positioning of the optical microprobe.

Classical mosaicing algorithms do not take into account the characteristics of fibered confocal microscopy, namely motion distortions, irregularly sampled frames and non-rigid deformations of the imaged tissue. In this section, we present some key points of the algorithms we developed in [26, 27] to address this problem.

19.6.1 Overview of the algorithm

Our approach in [27] is based on a hierarchical framework that is able to recover a globally consistent alignment of the input frames onto a reference coordinate system, to compensate for the motion-induced distortion of the input frames and to capture the non-rigid deformations of the tissue. Similarly to the velocimetry problem and the region of interest tracking problems presented above, we use the specificity of FCM to model and use the relationship between the motion distortions and the motion of the optical microprobe. As in (19.6), the displacement of the optical microprobe across the tissue can be described by a rigid shift denoted by r_n. The motion distortion can be modeled by a linear transformation v_n. Finally, due to the interaction of the contact optical microprobe with the soft tissue, a small non-rigid deformation b_n appears. The frame-to-reference mappings are thus modeled by:

$$f_n(p) = b_n \circ r_n \circ v_n(p). \tag{19.7}$$

The goal of the mosaicing algorithm is to recover these transformations for each frames.

A typical approach for dealing with the estimation of such complex models is to have a hierarchical, coarse-to-fine, approach. We therefore focus on a method that iteratively refines the model while always keeping the global consistency of the estimated frame-to-reference transformations.

From Local To Global Alignment – We start by assuming that the motion distortions as well as the non-rigid tissue deformations can be ignored. By making the reasonable assumption that consecutive frames are overlapping, an initial estimate of the global rigid mappings can be obtained by using a rigid registration technique to estimate the motion between the consecutive frames. Global alignment is then obtained by composing the local motions. This initial estimate suffers from a well-known accumulation of error problem that needs to be taken into account.

The first loop of our algorithm alternates between three steps. The first step of this loop assumes that the motion distortions have been correctly estimated and registers pairs of distortion compensated frames under a rigid body transformation assumption. The second step of the loop uses these local pairwise registration results to make a globally consistent estimation of the rigid mappings r_n. The third step uses the relationship between the motion and the motion distortions to provide an updated and consistent set of rigid mappings and motion compensations.

Let us focus on the second step of the first loop. During this local to global alignment scheme, we use all available pairwise rigid registration results to estimate a set of globally consistent transformations. A sound choice is to consider a least-square approach. However the space of rigid body transformations is not a vector space but rather a Lie group that can be considered as a Riemannian manifold. Classical notions using distances are therefore not trivial to generalize. In our work, we propose to cast this problem into an estimation problem on a Lie group.

By using the log map, we can define the (geodesic) distance between two rigid body transformations r and s as

$$\operatorname{dist}(r, s) = \operatorname{dist}\left(\mathrm{Id}, r^{-1} \circ s\right) = \|\log_{\mathrm{Id}}(r^{-1} \circ s)\| \tag{19.8}$$

In order to estimate the true rigid body transformations $[r_1, \ldots, r_N]$, we choose to minimize the distance between the observations $r_{j,i}^{(\mathrm{obs})} \in \Theta$ and the transformations $r_j^{-1} \circ r_i$ predicted by our model:

$$[r_1^*, \ldots, r_N^*] = \arg \min_{[r_1, \ldots, r_N]} \frac{1}{2} \sum_{(i,j) \in \Theta} \operatorname{dist}\left(r_j^{-1} \circ r_i, r_{j,i}^{(\mathrm{obs})}\right). \tag{19.9}$$

Note that further improvements to this formulation can be made. Mahalanobis distance and robust statistics can be used. It is also possible to weight the different registration results. An efficient optimization scheme is proposed in [26] to solve this estimation problem.

Mosaic Construction and Tissue Deformation Compensation – Once a globally consistent set of transformations is found, the algorithm constructs a point cloud by mapping all observed sampling points onto a common reference coordinate system. An efficient scattered data fitting technique is then used on this point cloud to construct an initial mosaic. The residual non-rigid deformations are finally taken into account by a second loop in our algorithm that iteratively registers an input frame to the mosaic and updates the mosaic based on the new estimate of the frame-to-mosaic mapping. The non-rigid registration can typically use the diffeomorphic registration scheme we present in [28].

Let us now get some insight into the efficient scattered data fitting technique we developed. Let $\{(p_k, i_k) \in \Omega \times \mathbb{R}\}$ be the set of sampling points and their associated signal. Our goal is to get an approximation of the underlying function on a regular grid Γ defined in Ω. The main idea is to use a method close to Shepard's interpolation. The value associated with a point in Γ is a weighted average of the nearby sampled values,

$$\hat{I}(p) = \sum_k w_k(p) i_k = \sum_k \frac{h_k(p)}{\sum_l h_l(p)} i_k. \tag{19.10}$$

The usual choice is to take weights that are the inverse of the distance, $h_k(p) = \mathrm{dist}(p, p_k)^{-1}$. In such a case we get a true interpolation [16]. An approximation is obtained if a bounded weighting function $h_k(p)$ is chosen. We choose a Gaussian weight $h_k(p) = G(p - p_k) \propto \exp(-||p - p_k||^2/2\sigma_a^2)$ and (19.10) can thus be rewritten as

$$\hat{I}(p) = \frac{\sum_k i_k G(p - p_k)}{\sum_k G(p - p_k)} = \frac{[G \star \sum_k i_k \delta_{p_k}](p)}{[G \star \sum_k \delta_{p_k}](p)}, \tag{19.11}$$

where δ_{p_k} is a Dirac distribution centered at p_k and $\star$ denotes a spatial convolution. We can see from this formulation that our reconstruction method thus only need two convolutions (Gaussian smoothing) and one division, which makes it very efficient.

19.6.2 Results and evaluation

As mentioned earlier, the issue of algorithm validation is critical in the field of biomedical imaging and usually requires dedicated and sophisticated approaches. In order to evaluate our global positioning and motion distortion compensation framework, image sequences of a rigid object were acquired in [27]. The object needs to have structures that can be seen with the fibered confocal microscope. For the mosaicing to be of interest, we also need to see shapes whose sizes are larger than the field of view of our imaging device. We therefore choose to image a silicon wafer.

A fair evaluation can only be made by comparing the output of the algorithm with independent information. Apart from simulated data, a ground truth of the imaged region is very difficult to get. Even with a standard microscope having a comparable resolution but a greater FOV it is not easy to see on the wafer whether the exact same region is being imaged or not. However, in addition to the mosaic, our algorithm also provides an estimation of the motion of the flexible microprobe. The evaluation framework we designed compares this estimation with a gold standard given by a computer numerical control (CNC) milling machine. The CNC milling machine is used to hold the flexible microprobe and prescribe, with respect to the silicon wafer, a motion whose accuracy is of the order of magnitude of the apparent fiber inter-core distance d_{ic}. We find that the motion recovered by our algorithm agrees with the prescribed one within a 3% error margin.

From the application point of view, mosaicing for fibered confocal microscopy provides a step to bridge the gap between microscopic and macroscopic scales. Cellvizio® offers a new way to image and characterize several types of tissue. In many cases, mosaicing can help move beyond the limitations of FCM by offering an extended field of view. Our method has been successfully applied to many types of sequences acquired in both small animal and human tissue. We provide some insight of this by showing the result of our algorithm on some typical images.

Figure 19.8a shows a mosaic constructed from 21 input frames, each with a FOV of 417 µm by 297 µm. On this figure, we can see mouse tumoral angiogenesis. The need for *in vivo* imaging is urgent in this field. It can indeed help assess the efficiency of angiogenesis therapy [29]. Mosaicing techniques can further help in getting objective quantitative measurements. The result shown in figure 19.8b is of much clinical interest since it proves that obtaining a microscopic images of human lung tissue without any staining is feasible. Our mosaicing algorithm pushes this interest one step further by showing multiple alveolar structures in a single image. The mosaic in figure 19.8c, arising from 31 input frames, shows the tubular architecture of the kidney. In this setting, mosaicing could help getting trustful statistical shape measurements. Figure 19.8d shows the ability of Cellvizio® to image nervous tissue down to the dendritic endings and shows how mosaicing can help seeing many of those dendritic endings simultaneously. 70 input frames all with a FOV of 397 µm by 283 µm were used to produce the mosaic.

19.7 Conclusion

New imaging technologies such as fibered confocal microscopy raise several new image processing and image analysis challenges that cannot readily be addressed by using classical approaches. In this paper several dedicated tools were presented. By taking into account the specificity of this imaging modality, the automated algorithms we developed lead to more physiologically relevant data, easier interpretation by the experts and provide an important step to bridge the gap between microscopic and higher resolution images like MRI, PET, SPECT or US.

Bibliography

[1] G. Bourg-Heckly, J. Blais, J. J. Padilla, O. Bourdon, J. Etienne, F. Guillemin, and L. Lafay, “Endoscopic ultraviolet-induced autofluorescence spectroscopy of the esophagus : Tissue characterization and potential for early cancer diagnosis,” *Endoscopy*, vol. 32, no. 10, pp. 756–765, 2000.

[2] P. Sharma, A. P. Weston, M. Topalovski, R. Cherian, A. Bhattacharyya, and R. E. Sampliner, “Magnification chromoendoscopy for the detection of intestinal metaplasia and dysplasia in Barrett’s oesophagus,” *Gut*, vol. 52, pp. 24–27, Jan. 2003.

[3] S.-E. Kudo, C. A. Rubio, C. R. Teixeira, H. Kashida, and E. Kogure, “Pit pattern in colorectal neoplasia: Endoscopic magnifying view,” *Endoscopy*, vol. 33, pp. 367–373, 2001.

[4] A. Meining, M. Bajbouj, S. Delius, and C. Prinz, “Confocal laser scanning microscopy for in vivo histopathology of the gastrointestinal tract,” *Arab Journal of Gastroenterology*, vol. 8, pp. 1–4, Mar. 2007.

[5] A. Hoffman, M. Goetz, M. Vieth, P. R. Galle, M. F. Neurath, and R. Kiesslich, “Confocal laser endomicroscopy: Technical status and current indications,” *Endoscopy*, vol. 38, pp. 1275–1283, Dec. 2006.

[6] H. Inoue, S. ei Kudo, and A. Shiokawa, “Technology insight: Laser-scanning confocal microscopy and endocytoscopy for cellular observation of the gastrointestinal tract,” *Nature Clinical Practice: Gastroenterology & Hepatology*, vol. 2, pp. 31–37, Jan. 2005.

[7] T. D. Wang, M. J. Mandella, C. H. Contag, and G. S. Kino, “Dual-axis confocal microscope for high-resolution in vivo imaging,” *Optics Letter*, vol. 28, pp. 414–416, Mar. 2003.

[8] K. Sokolov, J. Aaron, B. Hsu, D. Nida, A. Gillenwater, M. Follen, C. MacAulay, K. Adler-Storthz, B. Korgel, M. Descour, R. Pasqualini, W. Arap, W. Lam, and R. Richards-Kortum, "Optical systems for in vivo molecular imaging of cancer," *Technology in Cancer Research & Treatment*, vol. 2, pp. 491–504, Dec. 2003.

[9] K.-B. Sung, C. Liang, M. Descour, T. Collier, M. Follen, and R. Richards-Kortum, "Fiber-optic confocal reflectance microscope with miniature objective for in vivo imaging of human tissues," *IEEE Transactions on Biomedical Engineering*, vol. 49, pp. 1168–1172, Oct. 2002.

[10] B. A. Flusberg, E. D. Cocker, W. Piyawattanametha, J. C. Jung, E. L. M. Cheung, and S. M. J., "Fiber-optic fluorescence imaging," *Nature Methods*, vol. 2, pp. 941–950, Dec. 2005.

[11] F. Helmchen, "Miniaturization of fluorescence microscopes using fibre optics," *Experimental Physiology*, vol. 87, pp. 737–745, Nov. 2002.

[12] C. Winter, S. Rupp, M. Elter, C. Münzenmayer, H. Gerhäuser, and T. Wittenberg, "Automatic adaptive enhancement for images obtained with fiberscopic endoscopes," *IEEE Transactions on Biomedical Engineering*, vol. 53, pp. 2035–2046, Oct. 2006.

[13] M. Elter, S. Rupp, and C. Winter, "Physically motivated reconstruction of fiberscopic images," in *Proceedings of the 18th International Conference on Pattern Recognition (ICPR'06)*, (Hong Kong), pp. 599–602, Aug. 2006.

[14] G. Le Goualher, A. Perchant, M. Genet, C. Cavé, B. Viellerobe, F. Berier, B. Abrat, and N. Ayache, "Towards optical biopsies with an integrated fibered confocal fluorescence microscope," in *Proceedings of the 7th International Conference on Medical Image Computing and Computer Assisted Intervention (MICCAI'04)* (C. Barillot, D. R. Haynor, and P. Hellier, eds.), vol. 3217 of *Lecture Notes in Computer Science*, pp. 761–768, Springer-Verlag, 2004.

[15] S. K. Lodha and R. Franke, "Scattered data techniques for surfaces," in *Dagstuhl '97, Scientific Visualization*, (Washington, DC, USA), pp. 181–222, IEEE Computer Society, 1999.

[16] I. Amidror, “Scattered data interpolation methods for electronic imaging systems: A survey,” *Journal of Electronic Imaging*, vol. 11, pp. 157–176, Apr. 2002.

[17] S. Lee, G. Wolberg, and S. Y. Shin, “Scattered data interpolation with multilevel B-splines,” *IEEE Transactions on Visualization and Computer Graphics*, vol. 3, no. 3, pp. 228–244, 1997.

[18] E. Laemmel, M. Genet, G. Le Goualher, A. Perchant, J.-F. Le Gargasson, and E. Vicaut, “Fibered confocal fluorescence microscopy (Cell-viZio™) facilitates extended imaging in the field of microcirculation,” *Journal of Vascular Research*, vol. 41, no. 5, pp. 400–411, 2004.

[19] N. Savoire, G. Le Goualher, A. Perchant, F. Lacombe, G. Malandain, and N. Ayache, “Measuring blood cells velocity in microvessels from a single image: Application to *in vivo* and *in situ* confocal microscopy,” in *Proceedings of the IEEE International Symposium on Biomedical Imaging: From Nano to Macro (ISBI’07)*, pp. 456–459, Apr. 2004.

[20] Y. Sato, J. Chen, R. A. Zoroofi, N. Harada, S. Tamura, and T. Shiga, “Automatic extraction and measurement of leukocyte motion in microvessels using spatiotemporal image analysis,” *IEEE Transactions on Biomedical Engineering*, vol. 44, pp. 225–236, Apr. 1997.

[21] K. Krissian, G. Malandain, N. Ayache, R. Vaillant, and Y. Trousset, “Model-based detection of tubular structures in 3D images,” *Computer vision and image understanding*, vol. 80, pp. 130–171, Nov. 2000.

[22] A. Perchant, T. Vercauteren, F. Oberrietter, N. Savoire, and N. Ayache, “Region tracking algorithms on laser scanning devices applied to cell traffic analysis,” in *Proceedings of the IEEE International Symposium on Biomedical Imaging: From Nano to Macro (ISBI’07)*, (Arlington, USA), pp. 260–263, Apr. 2007.

[23] S. Benhimane and E. Malis, “Homography-based 2d visual tracking and servoing,” *International Journal of Robotics Research*, vol. 26, pp. 661–676, July 2007.

[24] T. Vercauteren, X. Pennec, E. Malis, A. Perchant, and N. Ayache, “Insight into efficient image registration techniques and the demons algorithm,”

in *Proceedings of Information Processing in Medical Imaging (IPMI'07)* (N. Karssemeijer and B. P. F. Lelieveldt, eds.), vol. 4584 of *Lecture Notes in Computer Science*, (Kerkrade, The Netherlands), pp. 495–506, Springer-Verlag, July 2007.

[25] K. Y. Lin, M. A. Maricevich, A. Perchant, S. Loiseau, R. Weissleder, and U. Mahmood, "Novel imaging method and morphometric analyses of microvasculature in live mice using a fiber-optic confocal laser microprobe," in *Proceedings of the Radiological Society of North America (RSNA'06)*, (Chicago, Il, USA), 2006.

[26] T. Vercauteren, A. Perchant, X. Pennec, and N. Ayache, "Mosaicing of confocal microscopic *in vivo* soft tissue video sequences," in *Proceedings of the 8th International Conference on Medical Image Computing and Computer Assisted Intervention (MICCAI'05)* (J. S. Duncan and G. Gerig, eds.), vol. 3749 of *Lecture Notes in Computer Science*, pp. 753–760, Springer-Verlag, 2005.

[27] T. Vercauteren, A. Perchant, G. Malandain, X. Pennec, and N. Ayache, "Robust mosaicing with correction of motion distortions and tissue deformation for *in vivo* fibered microscopy," *Medical Image Analysis*, vol. 10, no. 5, pp. 673–692, 2006. Annual MedIA/MICCAI Best Paper Award 2006.

[28] T. Vercauteren, X. Pennec, A. Perchant, and N. Ayache, "Non-parametric diffeomorphic image registration with the demons algorithm," in *Proceedings of the 10th International Conference on Medical Image Computing and Computer Assisted Intervention (MICCAI'07)* (N. Ayache, S. Ourselin, and A. J. Maeder, eds.), vol. 4792 of *Lecture Notes in Computer Science*, (Brisbane, Australia), pp. 319–326, Springer-Verlag, Oct. 2007.

[29] D. M. McDonald and P. L. Choyke, "Imaging of angiogenesis: From microscope to clinic," *Nature Medicine*, vol. 9, pp. 713–725, June 2003.

19.8 Grayscale Figures

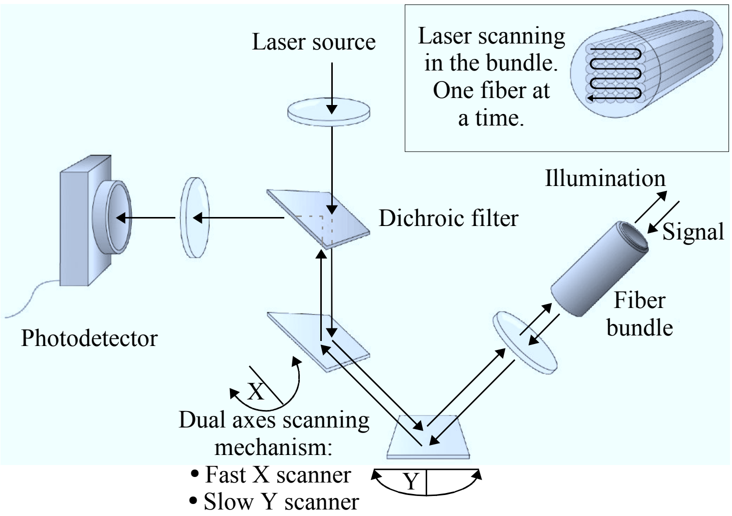

Figure 19.1: Schematic principle of fibered confocal microscopy.

19.9 Color Plate

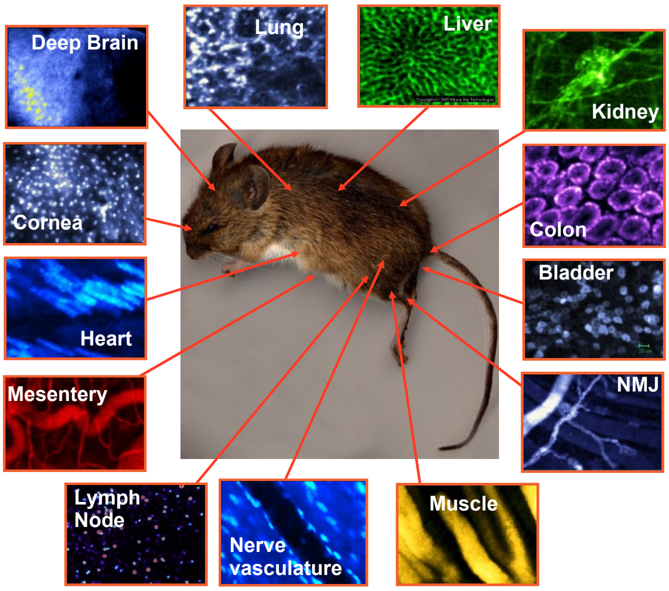

Figure 19.2: Different types of images from Leica FCM1000 microscope (Cellvizio® technology for small animal distributed by Leica microsystems).

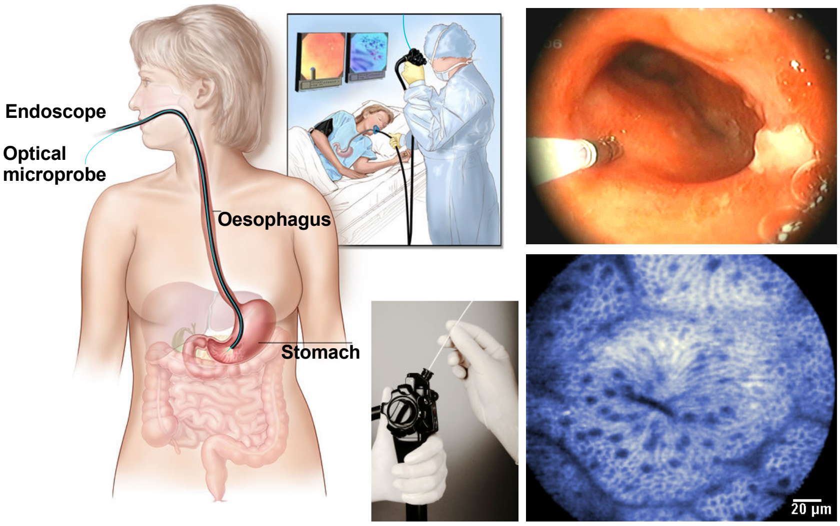

(a) (b)

Figure 19.3: Illustration of a typical Cellvizio®-GI setting. (a) The optical microprobe fits into the accessory channel of any endoscope. (b) Wide field-of-view imaging remains available when using Cellvizio®.

19.10 Grayscale Figures (continued)

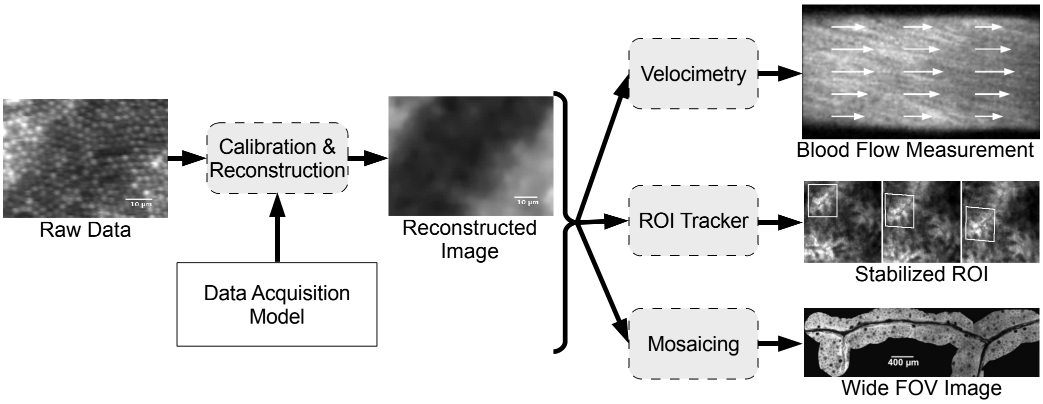

Figure 19.4: Some of the challenges involved in the processing of *in vivo* fibered confocal microscopy video sequences.

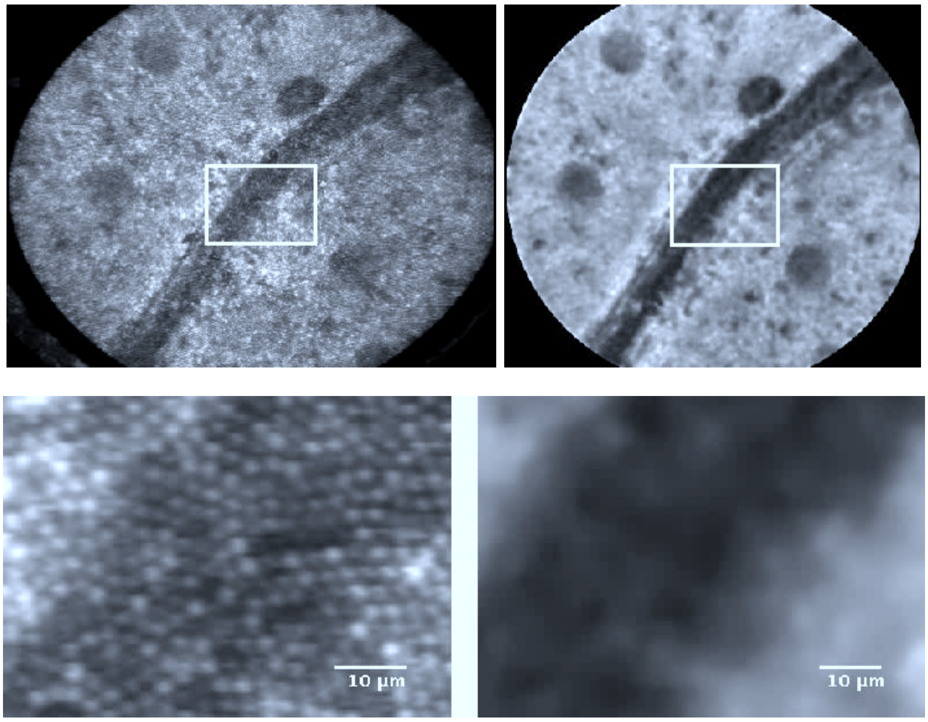

Figure 19.5: Autofluorescence FCM images of a Ficus Benjamina leaf. Left: Raw data. Right: Reconstructed images. Top: Complete images. Bottom: Zoom on rectangle. Note that the non-uniform honeycomb modulation and the geometric distortions on the raw data have been corrected in the reconstructed image.

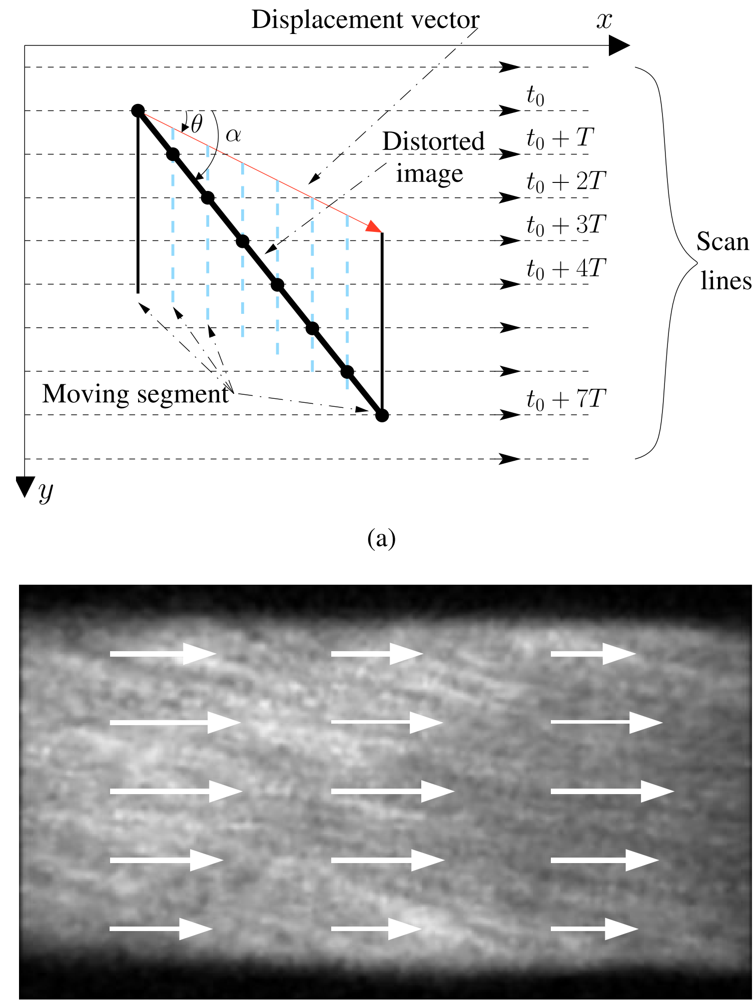

(a)

(b)

Figure 19.6: Blood Flow Velocimetry. (a) Imaging of a moving vertical segment by a scanning laser. The segment has a translation movement from the upper left corner to the lower right corner of the image. The segment is first intersected by a scan line at instant t_0 (black disks represent imaged points). The following scan lines image the segment at different positions (dotted segments). The resulting shape is the slanting segment of angle α. (b) *In vivo* mouse cremaster microvessel. The arrows are proportional to the estimated velocities computed on a block in the image. Note that, as expected, the velocity does not change along the direction of the microvessel and is maximal at the center.

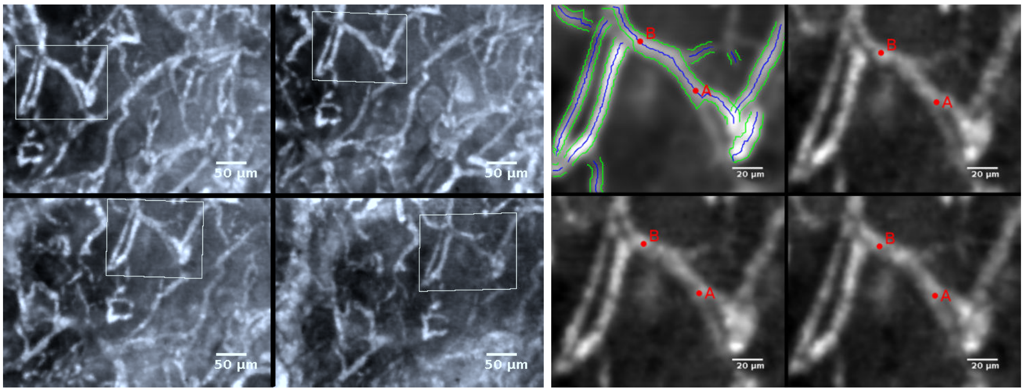

(a) (b)

Figure 19.7: (a) ROI tracking using affine transformations: 4 frames (index 1, 51, 101, 151) from the same sequence are displayed with the registered ROI. Complete sequence includes 237 frames. (b) Upper-left: vessel detection on the temporal mean frame after stabilization. Other images: three contiguous frames of the stabilized sequence (12 Hz). Blood velocity was acquired on the medial axis segment [AB].

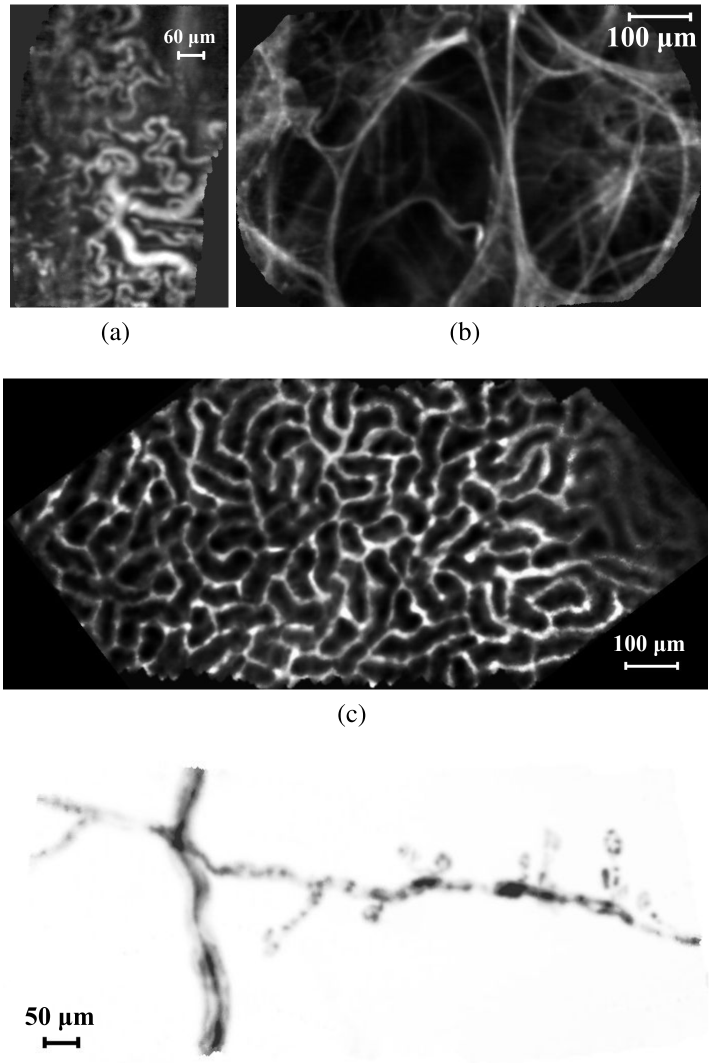

(a) (b)

(c)

(d)

Figure 19.8: Mosaics using different types of images acquired with Cellvizio®. (a) *In vivo* tumoral angiogenesis in mouse with FITC-Dextran high MW (21 input frames, courtesy of A. Duconseille and O. Clément, Université Paris V, Paris, France). (b) *Ex vivo* autofluorescence imaging in human lung (15 input frames, courtesy of Dr P. Validire, Institut Mutualiste Monsouris, Paris, France). (c) Microcirculation of the peritubular capillaries of a live mouse kidney with FITC-Dextran high MW (31 input frames). (d) Dendritic receptors in a live Thy1-YFP mouse (70 input frames, courtesy of I. Charvet, P. Meda, CMU, Geneva, Switzerland and L. Stoppini, Biocell Interface, Geneva, Switzerland).